

Unusual Strain Effect of Pt-Based L10 Face-Centered Tetragonal Core in Core/Shell Nanoparticles for Oxygen Reduction Reaction

M. Liu, Q. Wu

To be published in "PCCP"

February 2019

Center for Functional Nanomaterials
Brookhaven National Laboratory

U.S. Department of Energy
USDOE Office of Science (SC), Basic Energy Sciences (BES) (SC-22)

Notice: This manuscript has been authored by employees of Brookhaven Science Associates, LLC under Contract No. DE-SC0012704 with the U.S. Department of Energy. The publisher by accepting the manuscript for publication acknowledges that the United States Government retains a non-exclusive, paid-up, irrevocable, world-wide license to publish or reproduce the published form of this manuscript, or allow others to do so, for United States Government purposes.

DISCLAIMER

This report was prepared as an account of work sponsored by an agency of the United States Government. Neither the United States Government nor any agency thereof, nor any of their employees, nor any of their contractors, subcontractors, or their employees, makes any warranty, express or implied, or assumes any legal liability or responsibility for the accuracy, completeness, or any third party's use or the results of such use of any information, apparatus, product, or process disclosed, or represents that its use would not infringe privately owned rights. Reference herein to any specific commercial product, process, or service by trade name, trademark, manufacturer, or otherwise, does not necessarily constitute or imply its endorsement, recommendation, or favoring by the United States Government or any agency thereof or its contractors or subcontractors. The views and opinions of authors expressed herein do not necessarily state or reflect those of the United States Government or any agency thereof.

Unusual Strain Effect of Pt-Based L1₀ Face-Centered Tetragonal Core in Core/Shell Nanoparticles for Oxygen Reduction Reaction

Mingjie Liu^{†*}, Huolin Xin[†], Qin Wu^{†*}

[†] Center for Functional Nanomaterials, Brookhaven National Laboratory, Upton, NY, 11973

* Email: mliu@bnl.gov, qinwu@bnl.gov

Abstract: Nanoparticles with low-Pt content core and a few-layer Pt skin are attractive catalysts toward the oxygen reduction reaction (ORR) not only for its low cost, but also because its activity can be enhanced by judiciously choosing the core alloy. Achieving optimal ORR performance would require fine tuning of the core composition and structure. Previous work studying the enhancement effects has primarily focused on core alloys with a cubic structure, (i.e. disordered alloy or L1₂ ordered structure) which limits the tuning to composition alone. In this work, using ab initio calculations, we have systemically investigated a new class of Pt_{0.5}M_{0.5} (M=V, Cr, Fe, Co, Ni and Cu) core alloy that has a face-centered tetragonal L1₀ intermetallic structure. We have calculated the adsorption energies of O, OH, and OOH on various Pt skins and the underlying tetragonal structured alloys, which allows us to not only predict the optimal number of pure Pt skin layers but also tune the activity of the catalysts toward the peak of the ORR volcano plot. More importantly, using adsorption energies on intermediate structures, we are able to decompose the enhancement factor into ligand, normal and shear strain effects, and reveal the significant contribution of the shear strain that is only possible with a tetragonal core but not a cubic one. Our results point to a new direction in designing tetragonal structured intermetallic core-shell nanoparticles for ORR applications.

Key words: ORR, Pt-based alloy, core-shell, fct, DFT

Introduction:

Manipulating nanostructures to obtain desired properties is one of the goals in materials engineering. Take electrocatalysts in oxygen reduction reaction (ORR) as an example. In order to reduce the cost of currently used catalyst Pt and improve the efficiency, lots of efforts have been made to seek catalysts built from a core-shell architecture utilizing Pt-based bi- or multi-metallic nanoparticles.¹⁻³ In such structures, the shell is usually one or several atomic layers of Pt and the core could be a pure transition metal M, Pt-M alloy⁴⁻⁶ or multilayer alloy with one metal layers⁷.

The activity of the core-shell nanoparticles is greatly influenced by the shell configuration as well as the interaction between the shell and the core. To design the nanostructures at the molecular scale, we need to first understand the structure-activity relationship.⁸⁻¹⁰ There are typically three effects considered in designing the active surface¹¹: 1) the ensemble effect, where the surface atoms are composed with two or more elements¹²; 2) the ligand effect, where the surface electronic structure is modified by subsurface atoms¹³; 3) the geometric or strain effect, where the distances between surface atoms are changed¹⁴. Among them, the strain effect has been utilized most to optimize the performance of the catalysts,¹⁵⁻²⁰ e.g. the compressive strain is often used to shift the d-band center down so that the Pt/O* binding strength can be reduced, resulting in the improvement of Pt ORR activity.²¹ Volcano plot has been built to depict the correlation between the compressive strain and activity.¹⁵ In strain engineering, only under some specialized conditions, other factors need to be taken into consideration, e.g. ligand effect when the shell is too thin²² and relaxed strain if the shell is too thick¹⁸. Generally, designing the structure to obtain certain strain is the major approach to tune the catalyst activity. The usual way to engineer the strain is by exploiting the lattice mismatch through altering the type and ratio of M in Pt-M core. The strain of Pt shell can be tailored continuously to reach the desired level, effectively tuning the ORR activity.^{2, 18} However, such core configuration - Pt shell strain tuning so far is mostly limited to the simple case, where the core and shell share the identical face-centered cubic (fcc) structure. In that case, the compressive strain comes exclusively from introducing atoms with smaller radii than Pt to form ordered or disordered alloy.²³ In other words, such engineering strategy limits to tune the core composition alone. A slightly more complicated, yet much more interesting scenario, where the crystalline structure of the core differs from the shell, remains seldom explored, e.g. the structural transition occurs from the fcc core into the face-centered tetragonal (fct) intermetallic core²⁴⁻²⁶. For example, the nanocatalysts composed with Pt-Fe L1₀ fct phase as the core has been achieved with both better durability and superior activity than the disordered Pt-Fe L1₂ fcc phase.^{19, 24, 27-29} The fct Pt-Co nanoparticles have also been synthesized and revealed as the promising ORR catalysts recently.²⁹⁻³⁰ The intermetallic body-centered tetragonal structure of Pt-Fe-Cu as the electrocatalyst have been reported with improved activity and stability for methanol oxidation.³¹ It is thus of particular importance to gain deeper understanding of the fct Pt-M alloy core – Pt shell structure for ORR electrocatalysts.

In this work, we present our comprehensive study of the ORR catalytic activity of Pt-based 3d transition metal alloys, Pt_{0.5}M_{0.5} (M=V, Cr, Fe, Co, Ni, Cu), with fct crystalline core/Pt shell structure. The phase diagrams of the alloys can be found in the supporting information. The crystal structure of Pt_{0.5}V_{0.5} is orthorhombic (B19).³² The Pt_{0.5}Cu_{0.5} has a long-range order and the stable structure is rhombohedral (L1₁).³³⁻³⁴ For Cr, Fe, Co and Ni, the stable structures with Pt_{0.5}M_{0.5} are tetragonal L1₀.³⁵⁻³⁸ Although the L1₀ is the metastable structure for Pt_{0.5}V_{0.5} and Pt_{0.5}Cu_{0.5}, depending on the crystal growth approach, that metastable structure might be achieved such as using thin film deposition techniques³⁹. Therefore, we still include the V and Cu in our systematical study on the structural factors of L1₀ Pt-alloy (marked V and Cu with † denoting its metastable structure). Our investigation is based on thermodynamic factors, where the binding energy of intermediate species determines the activity of the catalyst, and the overpotential is originated from hindered proton and electron transfer to the stably adsorbed oxygen on Pt.⁴⁰ Under these approximations, the binding strength of intermediates can be referred as the activity descriptor. We use first principles calculations based on density functional theory (DFT) to probe their binding strengths. In the following, we first discuss the structural difference between fct (111) and fcc (111) surface for Pt_{0.5}M_{0.5}. A slab model of the fct Pt-M alloy substrate with few layers of Pt on top is used to simulate the fct core/Pt shell catalysts in ORR. Considering the associated mechanism where O₂ does not dissociate before it is hydrogenated, we then study the intermediates of O, OH and OOH adsorption on (111) surface of Pt-M (M=V, Cr, Fe, Co, Ni and Cu) with Pt layers on top, where the number of Pt layers varies from one to three. We compare the activity of these candidates using the criterion that the peak performance is reached when the O* binding energy is shifted by around 0.2 eV in reference to pure Pt (111).⁶ We further decompose the shift in binding energies and assign them to different effects for insights. Our results clearly show that the key distinction between fcc and fct is that in fct (111), there is not only in-plane normal strain, but also in-plane shear strain. Besides the additional strain effect, the fct structure gives rise to a subtle ligand effect due to the slight atomic position shift in stacking between layers. We have thus identified the key factors in the fct alloy core to the promising Pt shell catalytic activity for ORR performance. The enhancement factors are only possible with a tetragonal core but not a cubic one. More importantly, such factors are completely structural, and thus we expect them to be applicable to other fct alloys than Pt-M.

Method:

The DFT simulations are performed with Vienna *ab initio* simulation package (VASP).⁴¹ The PBE functional is used to describe the electron exchange and correlation⁴² with projector augmented wave (PAW) method.⁴³⁻⁴⁴ To obtain the fct alloy bulk lattice constant, series of total energies of the unit cell with various volumes are fitted with a 3rd order polynomial to get the optimized volume. Then the lattice was relaxed under constant volume to get the lattice parameters. The alloy (111) surface is modeled by a slab with 3 close-packed layers and the Pt skin of 1, 2, or 3 layers are added on top according to the substrate lattice structure. A (2×2) supercell is used which contains four atoms in each layer, completed with a vacuum layer of at least 15 Å. Spin polarization is included. The kinetic energy cutoff is 450 eV in plane-wave basis. The dipole correction is included in molecules adsorption calculations. The Brillouin zone is sampled with a 5×5×1 Monkhorst-Pack k-point mesh. The atoms in bottom layer are fixed while other atoms are relaxed until the force is less than 0.01 eV/ Å. The binding energy E_b is defined as

$$E_b(\text{O}^*) = E(\text{O}^*) - E(^*) - E(\text{H}_2\text{O}) + E(\text{H}_2);$$

$$E_b(\text{OH}^*) = E(\text{OH}^*) - E(^*) - E(\text{H}_2\text{O}) + 1/2E(\text{H}_2);$$

$$E_b(\text{OOH}^*) = E(\text{OOH}^*) - E(^*) - 2E(\text{H}_2\text{O}) + 3/2E(\text{H}_2);$$

Where $E(\text{X}^*)$ is the electronic energy of molecule adsorbed structure, $E(^*)$ is the electronic energy of substrate, $E(\text{H}_2\text{O})$ and $E(\text{H}_2)$ are the electronic energies of gas phase H_2O and H_2 molecules. We will compare the relative rather than absolute binding energy, therefore we have ignored the zero-point vibration and entropy effects because they are expected to be almost the same for different alloys in our calculations. We have verified this assumption by calculating the free energy ($\Delta G = \Delta E_{\text{ele}} + \Delta E_{\text{vib}} - T\Delta S$) of O^* adsorption on 3 Pt layers on fct-PtFe, PtCu and PtV structures; and found they differ from E_{ele} by less than 1%. While accurate prediction of the ORR activity will require solvation effect to be considered explicitly⁴⁵⁻⁴⁹, we have chosen not to include solvent here because our focus is on the subtle differences in materials properties, which should not depend on solvents.

Results and discussion:

In core-shell structure, the core induces a surface strain to the shell based on the lattice mismatch $S = ((a_{\text{shell}} - a_{\text{Pt}}) / a_{\text{Pt}}) \times 100\%$.¹⁵ If Pt-M forms chemically disordered fcc structure, the lattice is the average of bulk Pt and M according to Vegard's law. Alternatively, they can form an ordered fct intermetallic structure. The fct structure is illustrated in figure 1a, where $a = b \neq c$. The cubic to tetragonal lattice transition brings variation in corresponding surface structures. For example, the (100) surface of Pt-M undergoes anisotropic strain; and the (111) surface undergoes not only the normal strain, but also the shear strain compared with Pt (111). The unique shear strain only appears in (111) surface. Moreover, in Pt-alloy core/shell catalysts, the (111) surface is shown as the most active facet compared with (100).⁵⁰ Thus, in our study, we analyze the (111) facet first.

Figure 1b shows the unit cell of fct Pt-M (111) surface with two layers of Pt on top. In (111) surface with a (2×2) supercell, the lattice $l = \sqrt{(a^2 + c^2)}$ and $\gamma = 2 \arcsin\left(\frac{\sqrt{2}a}{2\sqrt{a^2 + c^2}}\right)$. The area of the cell is calculated as $\text{area} = l^2 * \sin(\gamma)$. For fcc structure, $c = a = b$, so $\gamma = 60^\circ$. When $c \neq a = b$, γ deviates from 60° , which means the Pt skin experiences both normal and shear strain from the fct substrate. Additionally, projection of atoms from different layers perpendicular to c axis no longer overlaps in fct, i.e. next-layer atom used to be in the center of the hollow site is now slightly off the center. This is due to different interlayer distances, i.e. stacking shifts, of Pt-M and Pt-Pt. Meanwhile, the thin Pt skin on top of the Pt-M alloy yields to the combined effects of in-plane strain and interlayer stacking shift of the substrate lattice. We have studied the fct structure of different 3d transition metals in $\text{Pt}_{0.5}\text{M}_{0.5}$, where M = V, Cr, Fe, Co Ni, and Cu. The lattice constants of the Pt-M are listed in Table 1. The parameters for unit cell of (111) surface are also listed. The normal strain in (111) is always compressive ($[l(\text{Pt-M}) - l(\text{Pt})] / l(\text{Pt}) < 0$), but the shear strain is compressive for V and Cr (i.e., $[\gamma(\text{Pt-M}) - \gamma(\text{Pt})] / \gamma(\text{Pt}) < 0$), and expansive for Fe, Co, Ni and Cu ($[\gamma(\text{Pt-M}) - \gamma(\text{Pt})] / \gamma(\text{Pt}) > 0$).

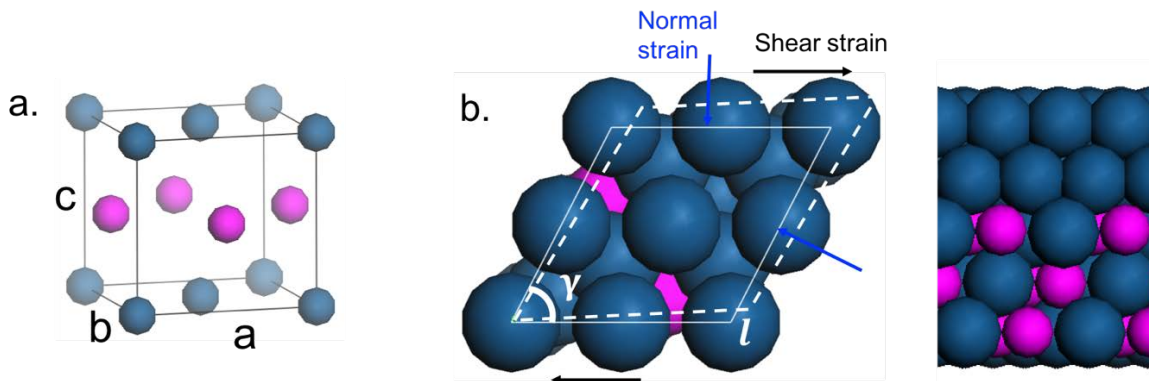


Table 1. the fct $\text{Pt}_{0.5}\text{M}_{0.5}$ alloy unit cell parameters.

M in Pt-M	$a=b$ (Å)	c (Å)	l (Å)	γ (°)	$[l(\text{Pt-M}) - l(\text{Pt})] / l(\text{Pt})$ (%)	$[\gamma(\text{Pt-M}) - \gamma(\text{Pt})] / \gamma(\text{Pt})$ (%)	$[\text{area}(\text{Pt-M}) - \text{area}(\text{Pt})] / \text{area}(\text{Pt})$ (%)
V [†]	3.83	3.91	5.47	59.31	-2.71	-1.14	-6.00
Cr	3.78	3.85	5.40	59.44	-4.07	-0.93	-8.49
Fe	3.86	3.77	5.40	60.77	-3.98	1.28	-7.11
Co	3.82	3.73	5.33	60.80	-5.16	1.33	-9.34
Ni	3.85	3.63	5.30	61.94	-5.85	3.23	-9.68
Cu [†]	3.94	3.61	5.34	62.85	-5.11	4.75	-7.49
Pt	3.98	3.98	5.62	60	0	0	0

The binding energies of $E_b(\text{O}^*)$, $E_b(\text{OH}^*)$ and $E_b(\text{OOH}^*)$ are investigated since they are important intermediate adsorbates in associative and dissociative mechanism. For each layer, binding structures of O, OH and OOH on different adsorption sites are optimized and the one with the lowest energy is used to calculate the binding energy. (Coordinates of all structures can be found in Supporting Information.)

We first examine the binding structures. Like in pure Pt, O^* prefers to adsorb on the hollow-fcc site⁵¹. For one and two Pt layers on top of Pt-M alloy, the energetically favorable hollow-fcc site for O^* is above Pt and M atom in the third layer, respectively. The most stable adsorption configuration for OH^* is oxygen on top of Pt and the O-H bond has an angle to the surface. This is different from pure Pt, where OH^* prefers the bridge site to top site, consistent with previous

reports for OH* on Pt (111) in vacuum,^{16, 52-54} although it also has been shown that when H₂O layers are considered, OH* prefers the top site^{48, 55-57}. The OOH* binds to the surface with oxygen on top of Pt, O-O bond on bridge site with O-H away from the surface; which agrees with that on pure Pt^{6, 16}.

Next we compare binding energies. As the Pt skin thickness increases from one to three layers, the binding strengths of all adsorbates approach their corresponding values on pure Pt, as expected. As shown in Figure 2a, binding strengths of O*, OH* and OOH* follow the scaling relationship with the fit of $E_b(\text{O}^*) = 1.88E_b(\text{OH}^*) - 0.15$ and $E_b(\text{OOH}^*) = 0.94E_b(\text{OH}^*) + 3.10$. It agrees with previous reports, where the OH* vs OOH* line has a slope around 1 and O* vs OH* has a slope close to 2 for metal-center porphyrin-like graphene, metal oxide and transition metal surface⁵⁸⁻⁶¹. Because of this scaling relationship, the knowledge of either O* OH* or OOH* adsorption energy is enough for the estimation of the surface activity^{6, 23, 40, 62-64}. Recent studies have shown that OH* binding energy as a descriptor gives maximal prediction efficiency for the ORR overpotential⁶⁵⁻⁶⁶. In this work, we still choose O* binding to investigate the structure-activity relationship. This is mostly for computational efficiency because we have a large number of intermediate binding structures to calculate in the following decomposition analysis. The binding structure of O* is simple, while OH binding may require us to explore different O-H bond orientations on surface. Considering the scaling relationships shown above, we believe our choice of O* is a reasonable one.

Figure 2b shows $\Delta E_b(\text{O}^*)$ from one layer to three layers of Pt on various Pt-M substrates. The optimal $\Delta E_b(\text{O}^*)$ is proposed to be ~0.2 eV weaker than the O* binding energy at Pt (111), $E_b(\text{O}^*@\text{Pt})$, as reference,⁶ while any value between 0 and 0.4 eV can be potentially better than pure Pt. Although the binding is too weak for the one-layer Pt skin, it becomes stronger as the number of Pt skin layer increases. For three layers of Pt on Pt-V[†], Pt-Fe and Pt-Cu[†], the O* bonding is already very close to the target value 0.2 eV.

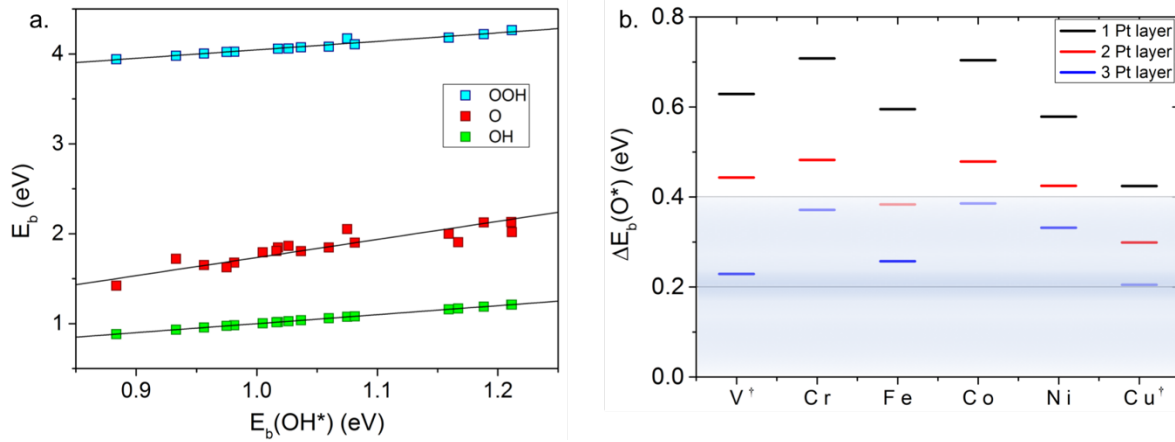


Figure 2. **a.** the scaling relationship of $E_b(\text{O}^*)$, $E_b(\text{OH}^*)$ and $E_b(\text{OOH}^*)$. The dashed lines are fitted linearly with $E_b(\text{O}^*) = 1.88E_b(\text{OH}^*) - 0.15437$ and $E_b(\text{OOH}^*) = 0.94E_b(\text{OH}^*) + 3.10$; The solid lines are fitted with fixed slope $E_b(\text{O}^*) = 2E_b(\text{OH}^*) - 0.27$ and $E_b(\text{OOH}^*) = E_b(\text{OH}^*) + 3.04$ in accordance with bond-order conservation principles. **b.** the $\Delta E_b(\text{O}^*)$ of Pt skin on Pt-M with different Pt-M ($\text{M} = \text{V}^\dagger$, Cr, Fe, Co Ni and Cu^\dagger) alloy and number of Pt skin layers (1-3 Pt layers). In activity volcano, the $\Delta E_b(\text{O}^*)$ from 0 to 0.4 eV using $E_b(\text{O}^*@\text{Pt})$ as reference are considered potential candidates possessing better activity than Pt, and 0.2 eV corresponds to the volcano peak⁶ which are highlighted with the light blue gradient in **b.**

Encouraged by these results, we next seek a better understanding of the structural factors that lead to the optimal $\Delta E_b(\text{O}^*)$. Ignoring the ensemble effect, which only applies to alloy surface, we focus on the ligand and the strain effects. In this system, the ligand effect originates from the vertical electronic structure modification by the alloy underneath, while the strain effect from the in-plane modification due to the lattice deformation. Compared with the near surface alloy (NSA) model used in simulation, where the ligand effect originates from the sublayer with a whole layer of solute metal^{13,67}, in intermetallic fct structure the ligand effect arises from the ordered Pt-M alloy surface, as well as the interlayer stacking shift, e.g. the atoms in the third layer are deviated from the center of fcc site (difference in structure is illustrated in figure 3b and c). The interlayer shifting can be recognized as the shear strain between layers. The relative position of atoms shifts in the in-plane direction. The strain effect here includes both the normal strain (changing l) and the shear strain (changing $\boldsymbol{\gamma}$). To quantify these effects, we propose to decompose the binding energy change, $\Delta E_b(\text{O}) = E_b(\text{O}^*@\text{fct-Pt-M}) - E_b(\text{O}^*@\text{fcc-Pt})$, in the following way:

$$\begin{aligned}\Delta E_b(O) &= \Delta E_b(\text{ligand}) + \Delta E_b(\text{strain}) \\ &= [E_b(\text{Pt-M@fct}) - E_b(\text{Pt@fcc}_\gamma)] + [E_b(\text{Pt@fcc}_\gamma) - E_b(\text{Pt@fcc})].\end{aligned}$$

Only O binding is considered and we have used the composition and structure of the core (linked by @) to indicate different systems. Therefore, $E_b(\text{Pt@fcc}_\gamma)$ is the O binding energy in Pt that has the fcc interlayer stacking (released interlayer shear strain) but with both in-plane shear and normal strain applied to the lattice (i.e., both l and γ are changed to fct Pt-M lattice parameter). In the above decomposition, the first term represents the ligand effect and it contains two consecutive transformations as illustrated in Figure 3. Starting from ordered Pt-M, the first step is to replace all M atoms with Pt atoms to construct a ‘pure Pt’ structure with Pt atoms fixed at the fct Pt-M coordinates (figure 3a to b). The second step is to release the interlayer shear strain where the stacking is identical to fcc structures (figure 3b to c). We attribute these two steps to pure ligand effect because there is no change to the position of the atoms in the surface layer. In the next two steps, we first release the in-plane shear strain, and then release the normal strain by restoring the lattice parameters to the pure Pt. We can then divide the strain effect into the shear (figure 3c to d) strain and normal (figure 3d to e) strain. Compared with fcc core, the terms arising from fct are the interlayer and in-plane shearing.

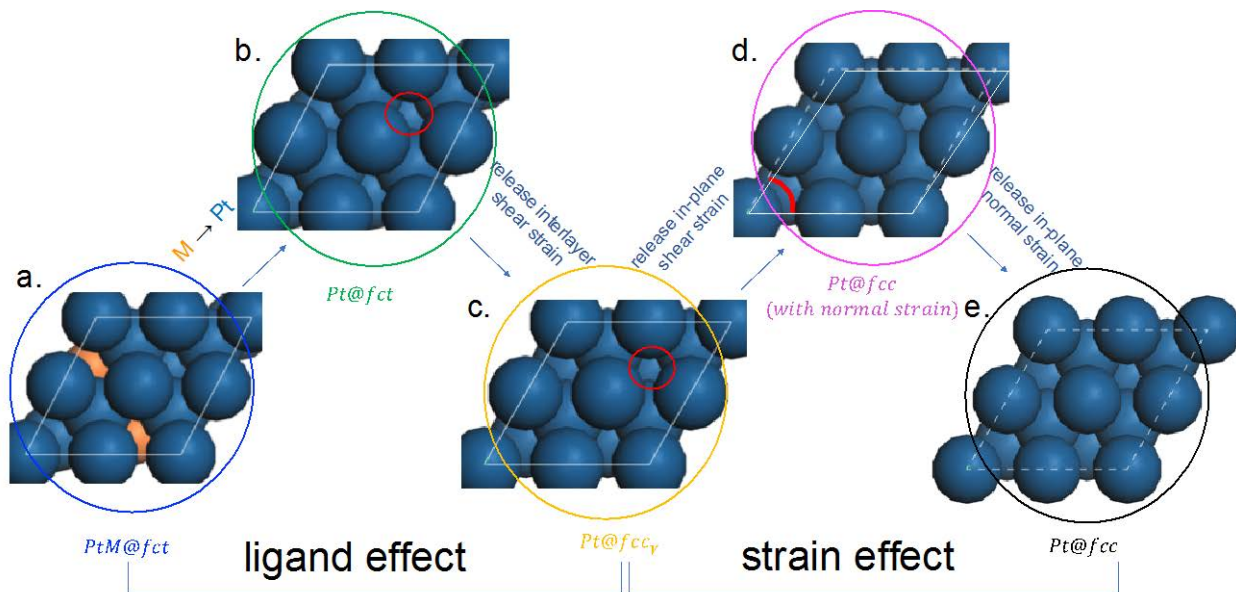


Figure 3. the intermediate structures used in energy decomposition. From Pt-M@fct, the first intermediate structure Pt@fct is derived by replacing all M with Pt without changing atoms’ position. The next intermediate structure Pt@fcc_γ is derived by releasing the interlayer shear strain with recovering the atoms stacking as that in fcc, preserving the in-plane normal and shear

strain. The Pt@fcc indicates Pt (111) with normal strain applied exclusively, where $\gamma=60^\circ$. The red marks in **b**, **c**, and **d** highlight the modeled structural change due to the interlayer and in-plane shearing.

The decomposed binding energy variations are shown in figure 4. As the number of Pt layers increases from one to three, the ligand effect decreases significantly while the strain effect only fluctuates within a narrow range (figure 4a-c). This is understandable because the surface/sublayer ligands quantum interaction should decay exponentially on their distance; on the other hand, surface strains can remain even at 5 layers above the core.⁶⁸ For the three-layer shell structures where the optimal E_b is found, it is apparent that strain is the dominant effect. If we use the surface area change of the unit cell to describe both the normal and shear strain, we find the strain effect is proportional to the surface area change, as shown in Figure 4d. The further decomposition of shear and normal strain is shown in figure S4. The normal strain is still the dominate effect while the expansive shear strain ($[\gamma(\text{Pt-M})-\gamma(\text{Pt})]/\gamma(\text{Pt})>0$) for Fe, Co Ni and Cu tune the O* binding energy in an opposite way. Although the shear strain effect is less dominated, it tunes the binding energy and move the activity closer to the optimal value. For instance, in the PtFe/Pt fct alloy, which was reported to have higher activity than fcc PtFe/Pt alloy¹⁹, even though our calculated shear strain effect only accounts for 0.03 ± 0.01 eV of the binding energy shift, it can explain all the difference between fcc and fct Pt-Fe.

With the decomposition of the binding energy variation, we can rationalize why the Pt-Cu fct alloy core-shell structure potentially has the best ORR activity. Cu atom is the smallest among these metals, and it makes the Pt lattice compressive normal strain reach 5% ($[l(\text{Pt-M})-l(\text{Pt})]/l(\text{Pt})$ in Table 1), exceeding the optimal value of 2%¹⁵. The shear strain on the other hand largely relieves the over-compressive normal strain by changing the unit cell shape. Pt-Cu has the largest shear strain effect of 0.11 ± 0.06 eV, which is critical in making the Pt-Cu fct potentially better than Pt-Fe fct. The ligand effect only plays a small role in countering the over-compression so as to make the binding energy optimal.

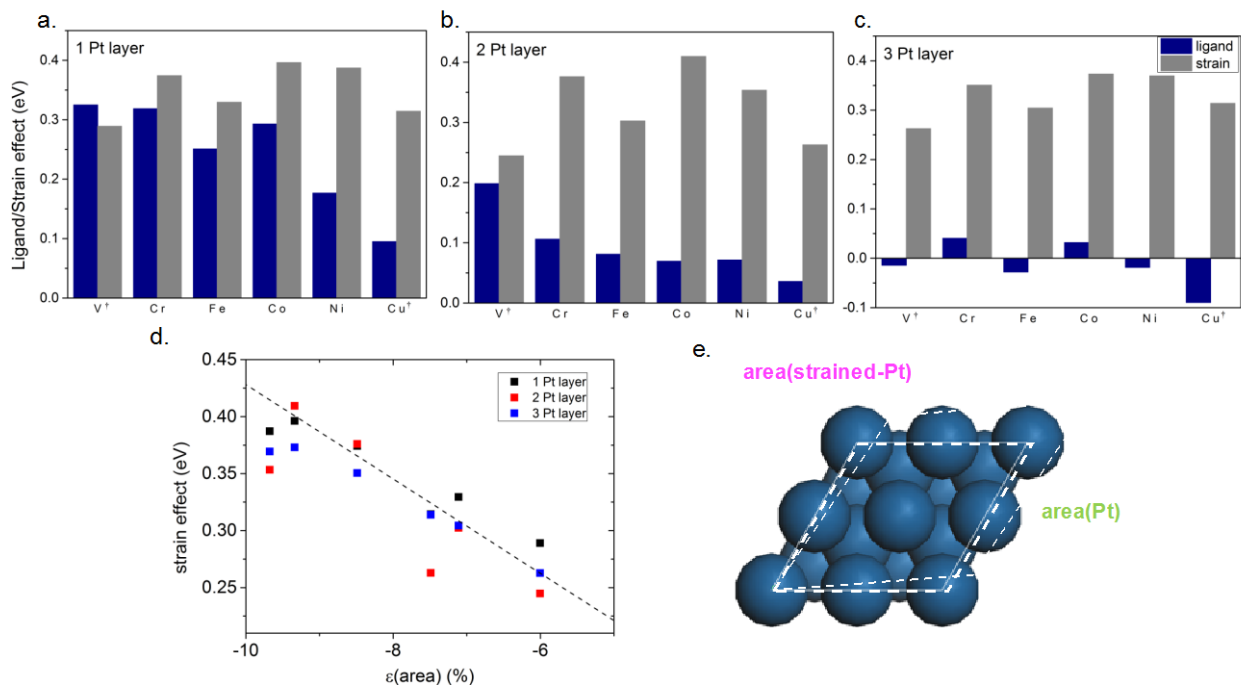


Figure 4. **a-c** the energy decomposed to ligand and strain effect for 1,2 and 3 Pt layers on fct-Pt-M; **d**, the strain effect for different Pt layers as a function of the (111) supercell surface area change as shown in **e**.

We have thus shown that the superior ORR activity of core-shell Pt nanoparticles with an ordered fct Pt-M alloy core comes mostly from the strain effect. Importantly, the fct core brings a shear strain to the (111) surface in addition to the normal strain that is commonly studied in fcc cores. The extra flexibility in tuning the Pt shell structure provided by the fct core can be potentially used to look for other intermetallic fct cores without Pt to further reduce Pt consumption. Indeed, the $L1_0$ tetragonal crystallographic structure is a flexible platform which offers versatile options of element combinations and ratios. The non-Pt alloy such as bulk Fe-Pd forms a $L1_0$ tetragonal structure with $c/a = 0.963$ ⁶⁹⁻⁷⁰. The fcc and fct transition happens for most In-alloy⁷¹⁻⁷². Moreover, the $L1_0$ tetragonal structure may be obtained not necessarily from the alloy with 1:1 component ratio. For example, Fe grown on Cu (100) at room temperature could form fct structure at certain condition.⁷³⁻⁷⁵ Those structures own different lattice parameters which could provide various normal and shear strain. Together with Pt skin, those fct structures could be of great interests to be utilized as the intermetallic core in core/shell structure.

Conclusion:

In conclusion, we carried out a detailed first-principles study on (111) surface of Pt-based alloy with ordered L1₀ fct intermetallic structure in core-shell architecture as the electrocatalyst for ORR. The oxygen binding energy has been used as a descriptor to determine the catalyst activity. To fully understand the fct structures, different facets, solvation effects, the transition states and other factors have to be considered to represent the whole catalysts reactivity picture.^{29, 48, 76} The layer thickness and component M in Pt-M alloy are as two variables to tune the surface towards the peak of ORR activity volcano. The structural factors have also been explored with the decomposition of strain and ligand effects in the fct core. The strain here not only contains the normal strain but also shear strain, which brings one more variable to control the structure-activity diagram. The ligand effect becomes trivial when there are more than three shell layers. It indicates that the fct core mainly provides the constrain geometrically. Therefore, the core can be chosen with other non-Pt fct intermetallic structure rather than Pt-based alloy to further reduce the usage of Pt. More importantly, the enhancement factor towards ORR activity works exclusively with a tetragonal core but not a cubic one. Our results reveal a new direction in designing core-shell nanoparticles with tetragonal structure and could facilitate further study of ordered intermetallic fct structure in ORR applications.

Acknowledgement:

This research is carried out at the Center for Functional Nanomaterials, which is a U.S. DOE Office of Science Facility, and used resource at the Scientific Data and Computing Center of the Computational Science Initiative, at Brookhaven National Laboratory under Contract No. DE-SC0012704.

References:

1. Oezaslan, M.; Hasche, F.; Strasser, P., Pt-Based Core-Shell Catalyst Architectures for Oxygen Fuel Cell Electrodes. *J Phys Chem Lett* **2013**, *4* (19), 3273-3291.
2. Koh, S.; Strasser, P., Electrocatalysis on bimetallic surfaces: Modifying catalytic reactivity for oxygen reduction by voltammetric surface dealloying. *Journal of the American Chemical Society* **2007**, *129* (42), 12624-+.
3. Wang, C.; Markovic, N. M.; Stamenkovic, V. R., Advanced Platinum Alloy Electrocatalysts for the Oxygen Reduction Reaction. *Acs Catalysis* **2012**, *2* (5), 891-898.

4. Wang, D.; Xin, H. L.; Hovden, R.; Wang, H.; Yu, Y.; Muller, D. A.; DiSalvo, F. J.; Abruña, H. D., Structurally ordered intermetallic platinum–cobalt core–shell nanoparticles with enhanced activity and stability as oxygen reduction electrocatalysts. *Nature Materials* **2012**, *12*, 81.
5. Stamenkovic, V. R.; Fowler, B.; Mun, B. S.; Wang, G.; Ross, P. N.; Lucas, C. A.; Marković, N. M., Improved oxygen reduction activity on Pt₃Ni (111) via increased surface site availability. *science* **2007**, *315* (5811), 493-497.
6. Greeley, J.; Stephens, I.; Bondarenko, A.; Johansson, T. P.; Hansen, H. A.; Jaramillo, T.; Rossmeisl, J.; Chorkendorff, I.; Nørskov, J. K., Alloys of platinum and early transition metals as oxygen reduction electrocatalysts. *Nature chemistry* **2009**, *1* (7), 552.
7. Van Cleve, T.; Moniri, S.; Belok, G.; More, K. L.; Linic, S., Nanoscale Engineering of Efficient Oxygen Reduction Electrocatalysts by Tailoring the Local Chemical Environment of Pt Surface Sites. *Acs Catalysis* **2017**, *7* (1), 17-24.
8. Nørskov, J. K.; Bligaard, T.; Rossmeisl, J.; Christensen, C. H., Towards the computational design of solid catalysts. *Nature chemistry* **2009**, *1* (1), 37.
9. Kulkarni, A.; Siahrostami, S.; Patel, A.; Norskov, J. K., Understanding Catalytic Activity Trends in the Oxygen Reduction Reaction. *Chem Rev* **2018**, *118* (5), 2302-2312.
10. Xin, H. L.; Holewinski, A.; Linic, S., Predictive Structure-Reactivity Models for Rapid Screening of Pt-Based Multimetallic Electrocatalysts for the Oxygen Reduction Reaction. *Acs Catalysis* **2012**, *2* (1), 12-16.
11. Gross, A., Tailoring the reactivity of bimetallic overlayer and surface alloy systems. *J Phys-Condens Mat* **2009**, *21* (8).
12. Chen, M. S.; Kumar, D.; Yi, C. W.; Goodman, D. W., The promotional effect of gold in catalysis by palladium-gold. *Science* **2005**, *310* (5746), 291-293.
13. Kitchin, J.; Nørskov, J. K.; Barteau, M.; Chen, J., Modification of the surface electronic and chemical properties of Pt (111) by subsurface 3d transition metals. *The Journal of chemical physics* **2004**, *120* (21), 10240-10246.
14. Mavrikakis, M.; Hammer, B.; Norskov, J. K., Effect of strain on the reactivity of metal surfaces. *Physical Review Letters* **1998**, *81* (13), 2819-2822.
15. Strasser, P.; Koh, S.; Anniyev, T.; Greeley, J.; More, K.; Yu, C.; Liu, Z.; Kaya, S.; Nordlund, D.; Ogasawara, H., Lattice-strain control of the activity in dealloyed core–shell fuel cell catalysts. *Nature chemistry* **2010**, *2* (6), 454.
16. Kattel, S.; Wang, G., Beneficial compressive strain for oxygen reduction reaction on Pt (111) surface. *The Journal of chemical physics* **2014**, *141* (12), 124713.
17. Moseley, P.; Curtin, W., Computational design of strain in core–shell nanoparticles for optimizing catalytic activity. *Nano letters* **2015**, *15* (6), 4089-4095.
18. Asano, M.; Kawamura, R.; Sasakawa, R.; Todoroki, N.; Wadayama, T., Oxygen reduction reaction activity for strain-controlled Pt-based model alloy catalysts: surface strains and direct electronic effects induced by alloying elements. *ACS Catalysis* **2016**, *6* (8), 5285-5289.
19. Zhang, S.; Zhang, X.; Jiang, G.; Zhu, H.; Guo, S.; Su, D.; Lu, G.; Sun, S., Tuning nanoparticle structure and surface strain for catalysis optimization. *Journal of the American Chemical Society* **2014**, *136* (21), 7734-7739.
20. Luo, M. C.; Guo, S. J., Strain-controlled electrocatalysis on multimetallic nanomaterials. *Nat Rev Mater* **2017**, *2* (11).

21. Stamenkovic, V.; Mun, B. S.; Mayrhofer, K. J.; Ross, P. N.; Markovic, N. M.; Rossmeisl, J.; Greeley, J.; Nørskov, J. K., Changing the activity of electrocatalysts for oxygen reduction by tuning the surface electronic structure. *Angewandte Chemie* **2006**, *118* (18), 2963-2967.
22. Stamenkovic, V. R.; Mun, B. S.; Mayrhofer, K. J. J.; Ross, P. N.; Markovic, N. M., Effect of surface composition on electronic structure, stability, and electrocatalytic properties of Pt-transition metal alloys: Pt-skin versus Pt-skeleton surfaces. *Journal of the American Chemical Society* **2006**, *128* (27), 8813-8819.
23. Colic, V.; Bandarenka, A. S., Pt Alloy Electrocatalysts for the Oxygen Reduction Reaction: From Model Surfaces to Nanostructured Systems. *Acs Catalysis* **2016**, *6* (8), 5378-5385.
24. Kim, J.; Lee, Y.; Sun, S., Structurally ordered FePt nanoparticles and their enhanced catalysis for oxygen reduction reaction. *Journal of the American Chemical Society* **2010**, *132* (14), 4996-4997.
25. Teng, X. W.; Yang, H., Synthesis of face-centered tetragonal FePt nanoparticles and granular films from Pt@Fe₂O₃ core-shell nanoparticles. *Journal of the American Chemical Society* **2003**, *125* (47), 14559-14563.
26. Yan, Y. C.; Du, J. S. S.; Gilroy, K. D.; Yang, D. R.; Xia, Y. N.; Zhang, H., Intermetallic Nanocrystals: Syntheses and Catalytic Applications. *Adv Mater* **2017**, *29* (14).
27. Li, Q.; Wu, L.; Wu, G.; Su, D.; Lv, H.; Zhang, S.; Zhu, W.; Casimir, A.; Zhu, H.; Mendoza-Garcia, A., New approach to fully ordered fct-FePt nanoparticles for much enhanced electrocatalysis in acid. *Nano letters* **2015**, *15* (4), 2468-2473.
28. Chung, D. Y.; Jun, S. W.; Yoon, G.; Kwon, S. G.; Shin, D. Y.; Seo, P.; Yoo, J. M.; Shin, H.; Chung, Y.-H.; Kim, H., Highly durable and active PtFe nanocatalyst for electrochemical oxygen reduction reaction. *Journal of the American Chemical Society* **2015**, *137* (49), 15478-15485.
29. Li, J.; Xi, Z.; Pan, Y.-T.; Spendelow, J. S.; Duchesne, P. N.; Su, D.; Li, Q.; Yu, C.; Yin, Z.; Shen, B.; Kim, Y. S.; Zhang, P.; Sun, S., Fe Stabilization by Intermetallic L10-FePt and Pt Catalysis Enhancement in L10-FePt/Pt Nanoparticles for Efficient Oxygen Reduction Reaction in Fuel Cells. *Journal of the American Chemical Society* **2018**, *140* (8), 2926-2932.
30. Jung, W. S.; Popov, B. N., New Method to Synthesize Highly Active and Durable Chemically Ordered fct-PtCo Cathode Catalyst for PEMFCs. *Acs Appl Mater Inter* **2017**, *9* (28), 23679-23686.
31. Zhu, J.; Yang, Y.; Chen, L. X.; Xiao, W. P.; Liu, H. F.; Abruna, H. D.; Wang, D. L., Copper-Induced Formation of Structurally Ordered Pt-Fe-Cu Ternary Intermetallic Electrocatalysts with Tunable Phase Structure and Improved Stability. *Chem Mater* **2018**, *30* (17), 5987-5995.
32. Waterstrat, R., The vanadium-platinum constitution diagram. *Metallurgical Transactions* **1973**, *4* (2), 455-466.
33. Mitsui, K.; Takahashi, M.; Takezawa, T., Effect of ternary addition on the formation of Cu₃Pt and CuPt order phases in the Cu-Pt system. *Phil Mag Lett* **1998**, *77* (1), 49-57.
34. Abe, T.; Sundman, B.; Onodera, H., Thermodynamic assessment of the Cu-Pt system. *J Phase Equilib Diff* **2006**, *27* (1), 5-13.
35. Venkatraman, M.; Neumann, J., The Cr-Pt (chromium-platinum) system. *Bulletin of Alloy Phase Diagrams* **1990**, *11* (1), 16-21.
36. Tibane, M. M. Phase stability study of Pt-Cr and Ru-Cr binary alloys. University of Limpopo (Turfloop Campus), 2011.

37. Franke, P.; Neuschütz, D., Co-Pt. In *Binary systems. Part 2: Elements and Binary Systems from B – C to Cr – Zr: Phase Diagrams, Phase Transition Data, Integral and Partial Quantities of Alloys*, Franke, P.; Neuschütz, D., Eds. Springer Berlin Heidelberg: Berlin, Heidelberg, 2004; pp 1-4.
38. Okamoto, H., Ni-Pt (nickel-platinum). *J Phase Equilib Diff* **2010**, *31* (3), 322-322.
39. Baglin, J.; Dheurle, F.; Zirinsky, S., Interactions between Cr and Pt Films - New Cr-Pt Phases. *J Electrochem Soc* **1978**, *125* (11), 1854-1859.
40. Nørskov, J. K.; Rossmeisl, J.; Logadottir, A.; Lindqvist, L.; Kitchin, J. R.; Bligaard, T.; Jonsson, H., Origin of the overpotential for oxygen reduction at a fuel-cell cathode. *The Journal of Physical Chemistry B* **2004**, *108* (46), 17886-17892.
41. Kresse, G.; Furthmuller, J., Efficient iterative schemes for ab initio total-energy calculations using a plane-wave basis set. *Phys Rev B* **1996**, *54* (16), 11169-11186.
42. Burke, K.; Ernzerhof, M.; Perdew, J. P., The adiabatic connection method: A non-empirical hybrid. *Chem Phys Lett* **1997**, *265* (1-2), 115-120.
43. Blochl, P. E., Projector Augmented-Wave Method. *Phys Rev B* **1994**, *50* (24), 17953-17979.
44. Kresse, G.; Joubert, D., From ultrasoft pseudopotentials to the projector augmented-wave method. *Phys Rev B* **1999**, *59* (3), 1758-1775.
45. Karlberg, G. S.; Rossmeisl, J.; Norskov, J. K., Estimations of electric field effects on the oxygen reduction reaction based on the density functional theory. *Phys Chem Chem Phys* **2007**, *9* (37), 5158-5161.
46. He, Z. D.; Hanselman, S.; Chen, Y. X.; Koper, M. T. M.; Calle-Vallejo, F., Importance of Solvation for the Accurate Prediction of Oxygen Reduction Activities of Pt-Based Electrocatalysts. *J Phys Chem Lett* **2017**, *8* (10), 2243-2246.
47. Tripkovic, V., Thermodynamic assessment of the oxygen reduction activity in aqueous solutions. *Phys Chem Chem Phys* **2017**, *19* (43), 29381-29388.
48. Sha, Y.; Yu, T. H.; Liu, Y.; Merinov, B. V.; Goddard, W. A., Theoretical Study of Solvent Effects on the Platinum-Catalyzed Oxygen Reduction Reaction. *J Phys Chem Lett* **2010**, *1* (5), 856-861.
49. Sha, Y.; Yu, T. H.; Merinov, B. V.; Shirvanian, P.; Goddard, W. A., Oxygen Hydration Mechanism for the Oxygen Reduction Reaction at Pt and Pd Fuel Cell Catalysts. *J Phys Chem Lett* **2011**, *2* (6), 572-576.
50. Han, B.; Viswanathan, V.; Pitsch, H., First-Principles Based Analysis of the Electrocatalytic Activity of the Unreconstructed Pt(100) Surface for Oxygen Reduction Reaction. *J Phys Chem C* **2012**, *116* (10), 6174-6183.
51. Xu, Y.; Ruban, A. V.; Mavrikakis, M., Adsorption and dissociation of O₂ on Pt–Co and Pt–Fe alloys. *Journal of the American Chemical Society* **2004**, *126* (14), 4717-4725.
52. Duan, Z. Y.; Wang, G. F., A first principles study of oxygen reduction reaction on a Pt(111) surface modified by a subsurface transition metal M (M = Ni, Co, or Fe). *Phys Chem Chem Phys* **2011**, *13* (45), 20178-20187.
53. Michaelides, A.; Hu, P., A density functional theory study of hydroxyl and the intermediate in the water formation reaction on Pt. *J Chem Phys* **2001**, *114* (1), 513-519.
54. Keith, J. A.; Jerkiewicz, G.; Jacob, T., Theoretical Investigations of the Oxygen Reduction Reaction on Pt(111). *Chemphyschem* **2010**, *11* (13), 2779-2794.

55. Schiros, T.; Naslund, L. A.; Andersson, K.; Gyllenpalm, J.; Karlberg, G. S.; Odelius, M.; Ogasawara, H.; Pettersson, L. G. M.; Nilsson, A., Structure and bonding of the water-hydroxyl mixed phase on Pt(111). *J Phys Chem C* **2007**, *111* (41), 15003-15012.
56. Clay, C.; Haq, S.; Hodgson, A., Hydrogen bonding in mixed OH+H₂O overlayers on Pt(111). *Physical Review Letters* **2004**, *92* (4).
57. Ogasawara, H.; Brena, B.; Nordlund, D.; Nyberg, M.; Pelmeshnikov, A.; Pettersson, L. G. M.; Nilsson, A., Structure and bonding of water on Pt(111). *Physical Review Letters* **2002**, *89* (27).
58. Abild-Pedersen, F.; Greeley, J.; Studt, F.; Rossmeisl, J.; Munter, T. R.; Moses, P. G.; Skulason, E.; Bligaard, T.; Norskov, J. K., Scaling properties of adsorption energies for hydrogen-containing molecules on transition-metal surfaces. *Physical Review Letters* **2007**, *99* (1).
59. Calle-Vallejo, F.; Krabbe, A.; Garcia-Lastra, J. M., How covalence breaks adsorption-energy scaling relations and solvation restores them. *Chem Sci* **2017**, *8* (1), 124-130.
60. Rossmeisl, J.; Qu, Z. W.; Zhu, H.; Kroes, G. J.; Norskov, J. K., Electrolysis of water on oxide surfaces. *J Electroanal Chem* **2007**, *607* (1-2), 83-89.
61. Rossmeisl, J.; Logadottir, A.; Norskov, J. K., Electrolysis of water on (oxidized) metal surfaces. *Chem Phys* **2005**, *319* (1-3), 178-184.
62. Bandarenka, A. S.; Hansen, H. A.; Rossmeisl, J.; Stephens, I. E. L., Elucidating the activity of stepped Pt single crystals for oxygen reduction. *Phys Chem Chem Phys* **2014**, *16* (27), 13625-13629.
63. Suo, Y. G.; Zhuang, L.; Lu, J. T., First-principles considerations in the design of Pd-alloy catalysts for oxygen reduction. *Angew Chem Int Edit* **2007**, *46* (16), 2862-2864.
64. Stephens, I. E. L.; Bondarenko, A. S.; Gronbjerg, U.; Rossmeisl, J.; Chorkendorff, I., Understanding the electrocatalysis of oxygen reduction on platinum and its alloys. *Energy Environ Sci* **2012**, *5* (5), 6744-6762.
65. Deshpande, S.; Kitchin, J. R.; Viswanathan, V., Quantifying Uncertainty in Activity Volcano Relationships for Oxygen Reduction Reaction. *ACS Catalysis* **2016**, *6* (8), 5251-5259.
66. Krishnamurthy, D.; Sumaria, V.; Viswanathan, V., Maximal Predictability Approach for Identifying the Right Descriptors for Electrocatalytic Reactions. *J Phys Chem Lett* **2018**, *9* (3), 588-595.
67. Stephens, I. E. L.; Bondarenko, A. S.; Perez-Alonso, F. J.; Calle-Vallejo, F.; Bech, L.; Johansson, T. P.; Jepsen, A. K.; Frydendal, R.; Knudsen, B. P.; Rossmeisl, J.; Chorkendorff, I., Tuning the Activity of Pt(111) for Oxygen Electroreduction by Subsurface Alloying. *Journal of the American Chemical Society* **2011**, *133* (14), 5485-5491.
68. Schlapka, A.; Lischka, M.; Gross, A.; Kasberger, U.; Jakob, P., Surface strain versus substrate interaction in heteroepitaxial metal layers: Pt on Ru(0001). *Physical Review Letters* **2003**, *91* (1).
69. Villars, P.; Calvert, L., Pearson's Handbook of Crystallographic Data for Intermediate Phases. *American Society of Metals, Cleveland, OH* **1985**.
70. Laughlin, D. E.; Srinivasan, K.; Tanase, M.; Wang, L., Crystallographic aspects of L10 magnetic materials. *Scripta Materialia* **2005**, *53* (4), 383-388.
71. Polovov, V. M.; Ponyatov, E. G., Thermodynamics of Face-Centered Tetragonal Face-Centered Cubic Transitions in Indium Alloys. *Zh Eksp Teor Fiz* **1973**, *64* (3), 937-945.

72. Degtyareva, O.; Degtyareva, V. F.; Porsch, F.; Holzapfel, W. B., Face-centred cubic to tetragonal transitions in In alloys under high pressure. *J Phys-Condens Mat* **2001**, *13* (33), 7295-7303.
73. Thomassen, J.; May, F.; Feldmann, B.; Wuttig, M.; Ibach, H., Magnetic live surface layers in Fe/Cu (100). *Physical review letters* **1992**, *69* (26), 3831.
74. Li, D.; Freitag, M.; Pearson, J.; Qiu, Z.; Bader, S., Magnetic phases of ultrathin Fe grown on Cu (100) as epitaxial wedges. *Physical review letters* **1994**, *72* (19), 3112.
75. Müller, S.; Bayer, P.; Reischl, C.; Heinz, K.; Feldmann, B.; Zillgen, H.; Wuttig, M., Structural instability of ferromagnetic fcc Fe films on Cu (100). *Physical review letters* **1995**, *74* (5), 765.
76. Li, M. F.; Zhao, Z. P.; Cheng, T.; Fortunelli, A.; Chen, C. Y.; Yu, R.; Zhang, Q. H.; Gu, L.; Merinov, B. V.; Lin, Z. Y.; Zhu, E. B.; Yu, T.; Jia, Q. Y.; Guo, J. H.; Zhang, L.; Goddard, W. A.; Huang, Y.; Duan, X. F., Ultrafine jagged platinum nanowires enable ultrahigh mass activity for the oxygen reduction reaction. *Science* **2016**, *354* (6318), 1414-1419.